# Structural and elastic anisotropy of crystals at high pressures and temperatures from quantum mechanical methods: The case of Mg2SiO4 forsterite

A. Erba, J. Maul, M. De La Pierre, and R. Dovesi

Citation: The Journal of Chemical Physics **142**, 204502 (2015); doi: 10.1063/1.4921781
View online: http://dx.doi.org/10.1063/1.4921781
View Table of Contents: http://scitation.aip.org/content/aip/journal/jcp/142/20?ver=pdfcov
Published by the AIP Publishing





# Structural and elastic anisotropy of crystals at high pressures and temperatures from quantum mechanical methods: The case of $Mg_2SiO_4$ forsterite

A. Erba,[1,a)] J. Maul,[1,2] M. De La Pierre,[3] and R. Dovesi[1]
[1]*Dipartimento di Chimica and Centre of Excellence NIS (Nanostructured Interfaces and Surfaces), Università di Torino, via Giuria 5, IT-10125 Torino, Italy*
[2]*Laboratório de Combustíveis e Materiais, INCTMN-UFPB, Universidade Federal da Paraíba, CEP 58051-900 João Pessoa, PB, Brazil*
[3]*Nanochemistry Research Institute, Curtin Institute for Computation, Department of Chemistry, Curtin University, GPO Box U1987, Perth, WA 6845, Australia*

(Received 27 March 2015; accepted 15 May 2015; published online 28 May 2015)

We report accurate *ab initio* theoretical predictions of the elastic, seismic, and structural anisotropy of the orthorhombic $Mg_2SiO_4$ forsterite crystal at high pressures (up to 20 GPa) and temperatures (up to its melting point, 2163 K), which constitute earth's upper mantle conditions. Single-crystal elastic stiffness constants are evaluated up to 20 GPa and their first- and second-order pressure derivatives reported. Christoffel's equation is solved at several pressures: directional seismic wave velocities and related properties (azimuthal and polarization seismic anisotropies) discussed. Thermal structural and average elastic properties, as computed within the quasi-harmonic approximation of the lattice potential, are predicted at high pressures and temperatures: directional thermal expansion coefficients, first- and second-order pressure derivatives of the isothermal bulk modulus, and *P-V-T* equation-of-state. The effect on computed properties of five different functionals, belonging to three different classes of approximations, of the density functional theory is explicitly investigated. © *2015 AIP Publishing LLC.* [http://dx.doi.org/10.1063/1.4921781]

## I. INTRODUCTION

Quantum-mechanical methods based on the Density Functional Theory (DFT) and on periodic-boundary conditions do represent an effective approach to the accurate description of fine features of a large variety of properties (such as structural, electronic, magnetic, spectroscopic, elastic, piezoelectric, and optical) of crystalline materials at ambient pressure and zero temperature.[1–6] Nowadays, one of the challenges, solid state computational approaches are facing, is that of extending their applicability domain and predictiveness to high pressure and temperature conditions. The effectiveness of DFT-based methods in describing structural and elastic properties of solids under pressure is well-known;[7] several techniques are available such as fitting energy-volume data to analytical expressions of the equation-of-state (EOS) of the system,[8,9] computing the analytical stress tensor and performing pressure-constrained geometry optimizations,[10,11] and correcting the fourth-rank elastic tensor according to its Lagrangian or Eulerian strain tensor formulation.[12–15] The description of thermal structural and elastic properties of crystals requires to go beyond the standard harmonic approximation to the lattice potential, whose limitations (including but not limited to zero thermal expansivity and temperature independence of elastic constants and bulk modulus) are well-known.[16,17] In this respect, due to its formal simplicity and relatively low computational cost, an effective method of choice is the so-called quasi-harmonic approximation (QHA), which introduces the missing volume dependence of phonon frequencies by retaining the harmonic expression for the Helmholtz free energy of the system.[18,19] A major advantage of such a scheme is that it allows for a natural combination of pressure and temperature on the same thermodynamic ground.

Among other fields, geophysics would particularly benefit from the knowledge of structural and elastic response of minerals at earth's mantle conditions (pressures up to 140 GPa and temperatures up to 2000 K),[20] as only such a full characterization of all the major constituents of the mantle could finally allow for a correct interpretation of seismological data and for the validation of different compositional models for the earth's deep interior which have been proposed so far.[21–24] From an experimental point of view, a large amount of X-ray diffraction studies were performed in past years in order to measure the isothermal equations of state of several rock-forming minerals to determine their *isotropic* equilibrium bulk modulus and its pressure and temperature derivatives.[25] If at ambient conditions, different experiments do agree with each other, very large differences among them are found at high temperatures and pressures, which prevent a reliable interpretation of seismic data.[26] The picture is even more unfavorable when considering the *anisotropic* characterization of the elastic and structural response of minerals, as experimental characterizations of their elastic tensor or directional thermal expansivity at simultaneous high pressure and temperature are extremely rare. In this

a)Electronic mail: alessandro.erba@unito.it

 

respect, quantum-mechanical methods (taking advantage of the techniques recalled above) offer a reliable alternative due to their high accuracy.[27,28]

Most crystals of the earth's mantle are structurally and elastically anisotropic; rocks from the mantle do show mineral preferred orientation and a large degree of alignment due to stress, flow fields, and high temperatures which make recrystallization a likely process.[20,29–31] It is now accepted that the top 200 km layer of the mantle behaves as an anisotropic medium on a global scale.[32] Elastic anisotropy gives rise to several subtle features such as the azimuthal anisotropy of both longitudinal and transverse seismic wave velocities (i.e., elastic wave velocities depend on propagation direction) and the shear-wave birefringence, that is, the two polarizations of transverse seismic waves do travel with different velocities with respect to each other. If disregarded, anisotropic effects can be interpreted as inhomogeneities such as layering or gradients.[30] The anisotropy of the upper mantle is mainly caused by the preferred orientation of olivine crystals, $(Mg_{1-x}Fe_x)_2SiO_4$, as induced by geodynamic phenomena. Olivine, indeed, is the most abundant mineral of the upper mantle, exhibits a large elastic anisotropy (for both longitudinal, about 25%, and transverse, about 18%, seismic waves), and is known to give rise to large areas with coherent crystal orientation. Forsterite, $\alpha$-$Mg_2SiO_4$, is an end-member of the olivine solid solution series and is one of the most abundant silicates in the upper mantle (its atomic structure is shown in Figure 1). It is stable up to about 14 GPa and 1300–1500 K; beyond these boundaries, it undergoes a phase transition to the $\beta$-$Mg_2SiO_4$ phase with wadsleyite structure.

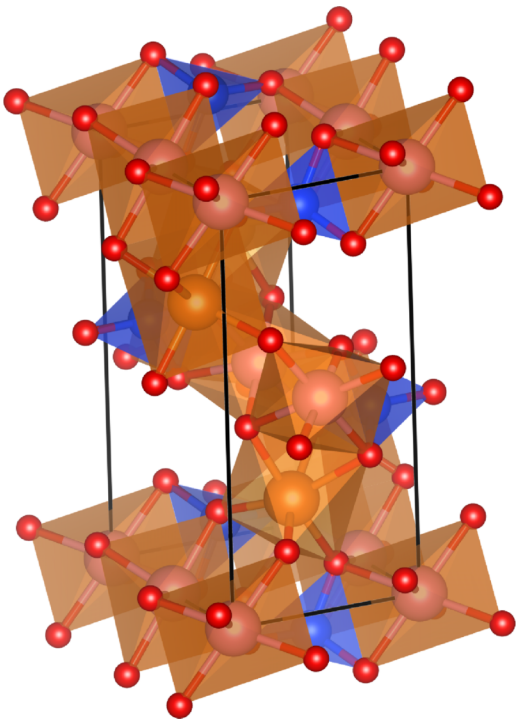

FIG. 1. Structure of the orthorhombic unit cell of $\alpha$-$Mg_2SiO_4$ forsterite. Oxygen atoms in red, magnesium atoms in brown, and silicon atoms in blue. $SiO_4$ tetrahedra and $MgO_6$ octahedra are also shown in brown and blue, respectively.

In this paper, we report about *ab initio* simulations of the structural and elastic response of forsterite at typical temperatures and pressures of the earth's upper mantle. The anisotropic thermal expansivity of $\alpha$-$Mg_2SiO_4$ is investigated through QHA calculations at simultaneous high $P$ and $T$ and its elastic and seismic anisotropies characterized up to 20 GPa. The temperature and pressure dependence of the adiabatic and isothermal bulk modulus of forsterite is also characterized. The effect of the particular choice of the exchange-correlation functional, within the DFT, on computed properties is explicitly investigated and documented by considering three different levels of approximation, corresponding to three rungs of the well-known "Jacob's ladder."[33] A development version of the CRYSTAL14 program[6] is used for all calculations where some of the present authors have recently implemented fully automated algorithms for the calculation of quasi-harmonic,[28,34,35] photo-elastic,[36] piezoelectric,[37,38] and elastic[15,39] properties of crystals.

The elasticity of single-crystal forsterite under pressure has been experimentally determined up to 4 GPa by Brillouin scattering,[40] up to 6 GPa by pulse-echo-overlap method,[41] up to 16 GPa by a Brillouin scattering experiment[42] (see also references therein for previous investigations), and simulated at the local density approximation (LDA) level of theory.[43–45] Several X-ray diffraction experiments have investigated the *anisotropic* thermal expansivity of forsterite at ambient pressure;[46–49] a relatively recent X-ray diffraction experiment by Katsura *et al.*, performed in a Kawai-type multi-anvil apparatus, has determined the thermal expansivity of forsterite at simultaneous high pressure, up to 14 GPa, and high temperature, up to 1900 K.[50] A couple of previous theoretical studies have described the *isotropic* thermal expansivity of forsterite.[51,52]

The structure of the paper is as follows. Section II is devoted to the illustration of the adopted computational setup and techniques for pressure-constrained geometry optimizations, elastic tensor calculation and evaluation of thermal structural properties within the quasi-harmonic approximation. In Sec. III, we discuss the elastic and seismic anisotropies of forsterite under pressure, its structural anisotropy, and its bulk modulus evolution at simultaneous high pressures and temperature. Conclusions are drawn in Sec. IV.

## II. METHODOLOGY AND COMPUTATIONAL SETUP

All the calculations reported in this study have been performed with algorithms implemented in a development version of the CRYSTAL14 program.[6] An all-electron atom-centered Gaussian-type-function (GTF) basis set is used for all atoms; silicon, oxygen, and magnesium atoms are described by (8$s$) (6311$sp$) (1$d$), (8$s$) (411$sp$) (1$d$), and (8$s$) (511$sp$) (1$d$) contractions of primitive GTFs, respectively. The exponents (in bohr$^{-2}$ units) of the most diffuse $sp$ shells are 0.32 and 0.13 (Si), 0.59 and 0.25 (O), and 0.68 and 0.22 (Mg); the exponents of the $d$ shells are 0.6 (Si), 0.5 (O), and 0.5 (Mg). The same basis set has already been successfully utilized in a couple of recent *ab initio* studies of vibrational and spectroscopic properties of forsterite.[53,54] In order to check whether or not the (8$s$) contraction of the 1$s$ core orbitals could affect the description

of the system under high pressures, a full de-contraction of the 1*s* orbitals of all atoms has also been explored, which, as expected, resulted in a constant lowering of the energy as a function of the compression, thus leaving all relative quantities (equilibrium volume, bulk modulus, etc.) unchanged.

Five different formulations of the exchange-correlation functional of the DFT are considered, corresponding to some of the most widely used schemes within the LDA, such as the SVWN functional,[55,56] the generalized-gradient approximation (GGA), such as the PBE[57] and PBEsol[58] functionals, and hybrid approaches, such as the B3LYP[59] and PBE0[60] functionals. Thresholds controlling the accuracy of Coulomb and exchange series are set to default values.[61] Reciprocal space is sampled using a Monkhorst-Pack mesh with a shrinking factor of 6 for the primitive cell of forsterite, corresponding to 64 independent $k$-points in the irreducible portion of the Brillouin zone. A pruned grid with 1454 radial and 99 angular points is used to calculate the DFT exchange-correlation contribution through numerical integration of the electron density over the unit cell volume.[61] The Self-Consistent-Field (SCF) convergence on energy was set to a value of $10^{-10}$ hartree for all geometry optimizations and phonon frequency calculations.

### A. Pressure-constrained structure optimization

A fully analytical scheme, based on the stress tensor, is used for optimizing the crystal volume under a given external pressure.[11] The stress tensor $\boldsymbol{\sigma}$ is a symmetric second-rank tensor that can be computed in terms of analytical energy gradients with respect to lattice parameters,

$$\sigma_{ij} = \frac{1}{V}\frac{\partial E}{\partial \epsilon_{ij}} = \frac{1}{V}\sum_{k=1}^{3}\frac{\partial E}{\partial a'_{ki}}a_{kj}, \tag{1}$$

with $\boldsymbol{\epsilon}$ second-rank symmetric pure strain tensor and $i,j,k = x,y,z$. In the second equality, $\partial E/\partial \epsilon_{ij}$ has been expressed in terms of analytical energy gradients with respect to lattice parameters of the strained lattice, whose calculation has been implemented in the CRYSTAL program about ten years ago by Doll *et al.* for 1D, 2D, and 3D periodic systems.[62,63] In the expression above, $a_{ij}$ are elements of a $3\times 3$ matrix, $\mathbf{A}$, where Cartesian components of the three lattice vectors $\mathbf{a}_1$, $\mathbf{a}_2$, and $\mathbf{a}_3$ are inserted by rows and $V$ is the cell volume. When a distortion is applied to the cell, the lattice parameters transform as $a'_{ij} = \sum_{k=1}^{3}(\delta_{jk} + \epsilon_{jk})a_{ik}$, where $\delta_{jk}$ is the Kronecker delta. Adding an external hydrostatic "pre-stress" $\sigma_{ij}^{\text{pre}} = -P\delta_{ij}$ to $\sigma_{ij}$ and inverting Eq. (1) yield to the following expression for the constrained gradients:

$$\frac{\partial H}{\partial a_{ij}} = \frac{\partial E}{\partial a_{ij}} + PV(\mathbf{A}^{-1})_{ji}. \tag{2}$$

With the inclusion of a hydrostatic pressure, the function to be minimized during the optimization process becomes the enthalpy, $H = E + PV$, of the system.[10]

### B. Elastic tensor calculation

If any finite pre-stress is absent, second-order elastic constants are simply defined as second energy density derivatives with respect to pairs of infinitesimal Eulerian strains,

$$C^0_{ijkl} = \frac{1}{V_0}\left(\frac{\partial^2 E}{\partial \epsilon_{ij}\partial \epsilon_{kl}}\right)_{\epsilon=0}. \tag{3}$$

A scheme for the calculation of the elastic tensor has been implemented in the CRYSTAL program[39,64] that has been generalized also to low-dimensionality, 1D and 2D, systems.[65]

When a finite pre-stress $\boldsymbol{\sigma}^{\text{pre}}$ is applied in the form of a hydrostatic pressure $P$, within the frame of finite Eulerian strain, the elastic stiffness constants become[12–14,66,67]

$$C_{ijkl} = C^0_{ijkl} + \frac{P}{2}(2\delta_{ij}\delta_{kl} - \delta_{il}\delta_{jk} - \delta_{ik}\delta_{jl}), \tag{4}$$

provided that $V_0$ in Eq. (3) is replaced by the equilibrium volume $V(P)$ at pressure $P$. An implementation in the CRYSTAL program of the calculation of the stiffness tensor $\mathbf{C}$ (and of $\mathbf{S} = \mathbf{C}^{-1}$, the compliance tensor) under pressure has recently been presented.[15,68,69] A two-index representation of the elastic stiffness tensor is obtained ($C_{ijkl} \rightarrow C_{vu}$) by exploiting Voigt's notation, according to which $v,u = 1,\ldots,6 (1 = xx,\ 2 = yy,\ 3 = zz,\ 4 = yz,\ 5 = xz,\ 6 = xy)$.[70] This tensor, in general, exhibits 21 independent elements that reduce to 9 in the case of orthorhombic crystals as forsterite. For the elastic constant calculation, two strained configurations are considered for each independent strain, with a dimensionless strain amplitude of 0.01 (i.e., 1%). From the knowledge of the elastic tensor, a number of elastic properties can be deduced.[70–72]

### C. Thermal structural properties

A fully automated scheme for computing quasi-harmonic properties of crystals has recently been implemented in the CRYSTAL program, which relies on computing and fitting (with a cubic polynomial function) harmonic vibration frequencies at different volumes after having performed volume-constrained geometry optimizations.[34,35] Harmonic phonon frequencies are computed by diagonalizing the dynamical matrix following a "direct space" approach.[34,73–75] Quasi-harmonic properties (such as the constant-pressure specific heat, the thermal expansion coefficient, or the temperature dependence of the bulk modulus) are computed by considering a volume range extending from a −6% compression to a +12% expansion with respect to the equilibrium volume; seven equidistant volumes are considered in this interval.

The *isotropic* thermal expansion coefficient, $\alpha_V(T)$, of the system is obtained by minimizing the isothermal Helmholtz free energy,

$$F^{\text{QHA}}(T,V) = U_0^{\text{ZP}}(V) + k_B T\sum_{\mathbf{k}p}\left[\ln\left(1 - e^{-\frac{\hbar\omega_{\mathbf{k}p}(V)}{k_B T}}\right)\right], \tag{5}$$

with respect to volume at several temperatures, where $k_B$ is Boltzmann's constant and $U_0^{\text{ZP}}(V)$ is the zero-temperature internal energy of the crystal which includes the zero-point energy of the system, $E_0^{\text{ZP}}(V) = \sum_{\mathbf{k}p}\hbar\omega_{\mathbf{k}p}(V)/2$. The *anisotropic* thermal expansion can be computed as well: directional thermal expansion coefficients, $\alpha_a(T)$, $\alpha_b(T)$, and $\alpha_c(T)$, corresponding to the $a$, $b$, and $c$ lattice parameters of

forsterite can be determined which allow for a finer description of the thermal expansion mechanism.[28]

The QHA allows for combining pressure and temperature effects on structural and elastic properties of materials. By differentiating Eq. (5) with respect to the volume and changing sign, the thermal pressure is obtained,

$$P(V;T) = -\frac{\partial F^{\mathrm{QHA}}(V;T)}{\partial V}. \quad (6)$$

The description of the isothermal bulk modulus of the system at simultaneous high-temperatures and high-pressures, $K_T(P,T)$, can be obtained as an isothermal second derivative of Eq. (5) with respect to the volume and by exploiting relation (6),

$$K_T(P,T) = V(P,T)\left(\frac{\partial^2 F^{\mathrm{QHA}}(V(P,T);T)}{\partial V(P,T)^2}\right)_T. \quad (7)$$

## III. RESULTS AND DISCUSSION

### A. Elastic anisotropy under pressure

As recalled in the Introduction, the top 200 km of the earth's upper mantle is known to behave as an anisotropic elastic medium as regards the propagation of seismic waves. In this respect, the large elastic anisotropy of olivine is believed to be the main responsible due to the high degree of crystal alignment. A detailed description of olivine anisotropy at upper mantle conditions is necessary in order to correctly interpret seismological data collected during earthquakes. The characterization of the elastic anisotropy of a crystal requires the determination of its elastic tensor: a fourth-rank symmetric tensor with 21 components (i.e., elastic constants) which reduce to 9 symmetry-independent ones for orthorhombic crystals such as olivine ($C_{11}$, $C_{22}$, $C_{33}$, $C_{44}$, $C_{55}$, $C_{66}$, $C_{12}$, $C_{13}$, and $C_{23}$). In the present study, we compute the full set of elastic constants of forsterite, the Mg-rich end-member of the olivine solid solution, at different pressures, up to 20 GPa. Before discussing into more detail some fine features of the elastic anisotropy of forsterite, we have to make sure that the overall elastic description of the system under increasing pressure is reliable as compared with available experimental data. In Figure 2, we report computed elastic stiffness constants, $C_{vu}$, of $Mg_2SiO_4$ forsterite as a function of pressure, up to 20 GPa (continuous lines). Experimental determinations are reported as well, as obtained from a couple of Brillouin scattering measurements by Zha *et al.*[42] up to 16 GPa (solid symbols), by Shimizu *et al.*[40] up to 4 GPa (crosses), and from a pulse-echo-overlap study up to 6 GPa by Yoneda and Morioka[41] (empty symbols). Some considerations are (i) apart from a slight underestimation of $C_{33}$, the absolute values of all elastic constants are accurately predicted by the calculations; (ii) all elastic constants do increase with pressure; (iii) the slope of all computed elastic constants with pressure agrees with experimental determinations, apart from a slight underestimation for $C_{55}$ and $C_{66}$; and (iv) experimental determinations of the elastic constants are not that regular as a function of pressure, particularly so at high pressures.

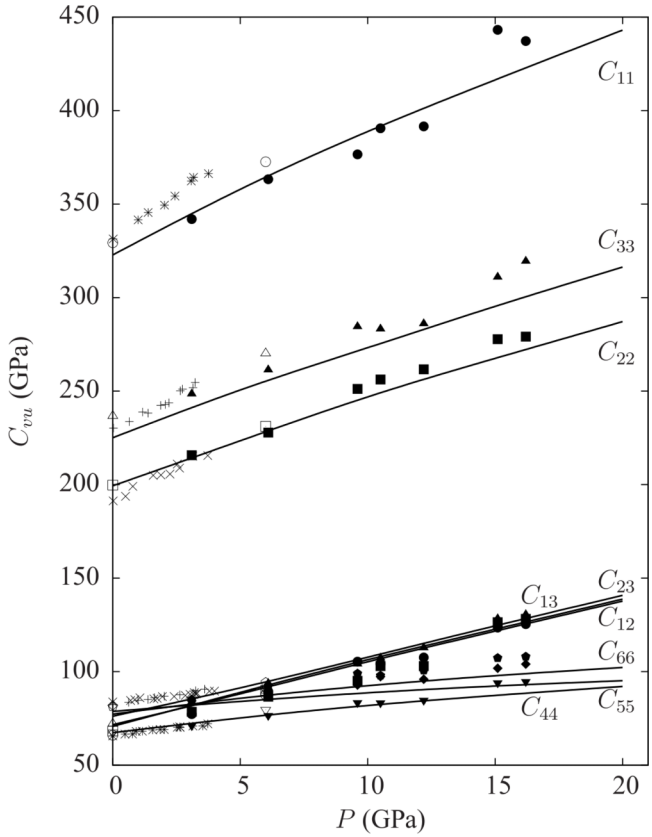


FIG. 2. Elastic stiffness constants of forsterite as a function of pressure, as computed at the PBE level of theory (continuous lines) and as experimentally determined by Zha *et al.*[42] (full symbols), Yoneda and Morioka[41] (empty symbols), and Shimizu *et al.*[40] (crosses).

In order to make a closer comparison with the experiment, let us introduce Table I, where we report the absolute values of the elastic constants at zero pressure, $C^0_{vu}$, along with their first-, $\mathrm{d}C_{vu}/\mathrm{d}P$, and second-derivatives, $\mathrm{d}^2C_{vu}/\mathrm{d}P^2$, with respect to pressure. Our computed values are compared with those reported by Yoneda and Morioka[41] in their accurate experimental study: (i) the overall agreement between computed and experimental zero pressure constants is remarkable; (ii) diagonal constants, from $C_{11}$ to $C_{66}$, are slightly underestimated, more so for $C_{33}$ than for the others; (iii) the agreement on first pressure derivatives, the main quantity to be considered in this kind of analysis, is rather satisfactory in all cases; and (iv) the agreement on second derivatives (*i.e.*, a very fine feature of the pressure dependence of the elastic constants) further confirms the high accuracy of present calculations. All second-derivatives are negative but that of the $C_{23}$ elastic stiffness constant. At variance with a previous *ab initio* simulation on the elasticity of forsterite under pressure that was unable to reproduce such a fine detail,[43] present results do correctly describe this feature. Present calculations do predict a large second-derivative of $C_{11}$ (−0.116) with respect to the experiment (−0.047); from inspection of Figure 2, it is clearly seen that this is due to the larger pressure range explored by present calculations as the curvature in the low-pressure regime is much smaller. In the last two rows of the table, the same data are reported for the average bulk, $\overline{K}$, and shear, $\overline{G}$, moduli. Elastic properties

TABLE I. Elastic constants of forsterite at zero pressure, $C^0_{vu}$, and their first- and second-derivatives with respect to pressure, as computed at the PBE level of theory and as compared with accurate experimental determinations by Yoneda and Morioka.[41] Data on the polycrystalline average bulk modulus, $K$ and shear modulus, $G$, as obtained from the Voigt-Reuss-Hill averaging scheme[76] are reported as well.

| | $C^0_{vu}$ (GPa) | | $dC_{vu}/dP$ | | $d^2C_{vu}/dP^2$ | |
|---|---|---|---|---|---|---|
| | Calc. | Expt. | Calc. | Expt. | Calc. | Expt. |
| $C_{11}$ | 323 | 329 | 7.13 | 7.22 | −0.116 | −0.047 |
| $C_{22}$ | 199 | 200 | 5.07 | 5.24 | −0.068 | −0.051 |
| $C_{33}$ | 225 | 237 | 5.09 | 5.57 | −0.054 | −0.094 |
| $C_{44}$ | 67 | 68 | 1.65 | 2.01 | −0.042 | −0.071 |
| $C_{55}$ | 79 | 82 | 1.16 | 1.46 | −0.034 | −0.021 |
| $C_{66}$ | 77 | 81 | 1.78 | 2.16 | −0.054 | −0.025 |
| $C_{12}$ | 71 | 66 | 3.70 | 3.59 | −0.030 | −0.009 |
| $C_{13}$ | 72 | 68 | 3.41 | 3.62 | −0.010 | −0.072 |
| $C_{23}$ | 76 | 72 | 3.10 | 2.94 | 0.016 | 0.077 |
| $\overline{K}$ | 129 | 129 | 4.12 | 4.19 | −0.030 | −0.018 |
| $\overline{G}$ | 78 | 81[a] | 1.40 | 1.4[b] | −0.042 | |

[a]The experimental value of the shear modulus from Suzuki *et al.*[77]
[b]First-order pressure derivative of the experimental shear modulus from Zha *et al.*[42]

of isotropic polycrystalline aggregates can be computed from the elastic and compliance constants via the Voigt-Reuss-Hill averaging scheme, for instance.[76] For crystals of any symmetry, the average bulk modulus $\overline{K} = 1/2[K_V + K_R]$ can be defined as an average between Voigt upper bound

$$K_V = \frac{1}{9}[C_{11} + C_{22} + C_{33} + 2(C_{12} + C_{13} + C_{23})]$$

and Reuss lower bound

$$K_R = [S_{11} + S_{22} + S_{33} + 2(S_{12} + S_{13} + S_{23})]^{-1}.$$

Similar expressions can be used to define the average shear modulus, $\overline{G}$.[70,71] The computed value of the average bulk modulus is 129 GPa and coincides with the experimental counterpart. As we will discuss below, however, this agreement partially comes from a cancellation of errors due to the fact that zero-point motion and thermal effects are neglected in the calculations while experimental data refer to ambient temperature. A rather satisfactory agreement with the experiment is also found on its first (4.12 compared with 4.19) and second (−0.0030 compared with −0.0018) pressure derivatives. A remarkable agreement is obtained also on the shear modulus and its first-order pressure derivative. As we shall discuss in Sec. III B, the inclusion of thermal effects will further increase the agreement on the bulk modulus pressure derivatives.

Let us now discuss the seismic anisotropy of forsterite and its evolution under increasing pressure. From a fundamental point of view, within the elastic continuum model, the velocity of propagation of a seismic wave traveling along any general crystallographic direction represented by unit wave-vector, $\hat{\mathbf{q}}$, can be obtained from the elastic tensor via Christoffel's equation, which can be given an eigenvalues/eigenvectors form as follows:[78,79]

$$\mathbf{A}^{\hat{\mathbf{q}}}\mathbf{U} = \mathbf{V}^2\mathbf{U}$$

with

$$A^{\hat{\mathbf{q}}}_{jk} = \frac{1}{\rho}\sum_{il}\hat{q}_i C_{ijkl}\hat{q}_l, \tag{8}$$

where $A^{\hat{\mathbf{q}}}_{jk}$ is Christoffel's matrix, $\rho$ is the crystal density, $i,j,k,l = x,y,z$ represent Cartesian directions, $\hat{q}_i$ is the $i$th element of the unit vector $\hat{\mathbf{q}}$, $\mathbf{V}$ is a $3\times3$ diagonal matrix whose three elements give the acoustic velocities, and $\mathbf{U} = (\hat{\mathbf{u}}_1, \hat{\mathbf{u}}_2, \hat{\mathbf{u}}_3)$ is the eigenvector $3\times3$ matrix where each column represents the polarization $\hat{\mathbf{u}}$ of the corresponding eigenvalue. The three acoustic wave velocities, also referred to as seismic velocities, can be labeled as quasi-longitudinal $v_p$, slow quasi-transverse $v_{s1}$ and fast quasi-transverse $v_{s2}$, depending on the polarization direction $\hat{\mathbf{u}}$ with respect to wave-vector $\hat{\mathbf{q}}$.[13] From the analysis of directional seismic wave velocities, the main aspects of the elastic anisotropy of a crystal, such as shear-wave birefringence and azimuthal anisotropy, can be fruitfully discussed, in particular as regards their evolution on pressure. In principle, from accurate single-crystal Brillouin scattering experiments, directional seismic wave velocities can be measured which convey the essential information for analyzing into detail the elastic anisotropy of a crystal. However, just a couple of directional studies have been performed so far for forsterite: by Yoneda and Morioka[41] at zero pressure and by Zha *et al.*[42] at 6.1 and 16.2 GPa. In Figure 3, we report our computed seismic wave velocities as a function of the crystallographic direction of propagation. Longitudinal and transverse wave velocities are

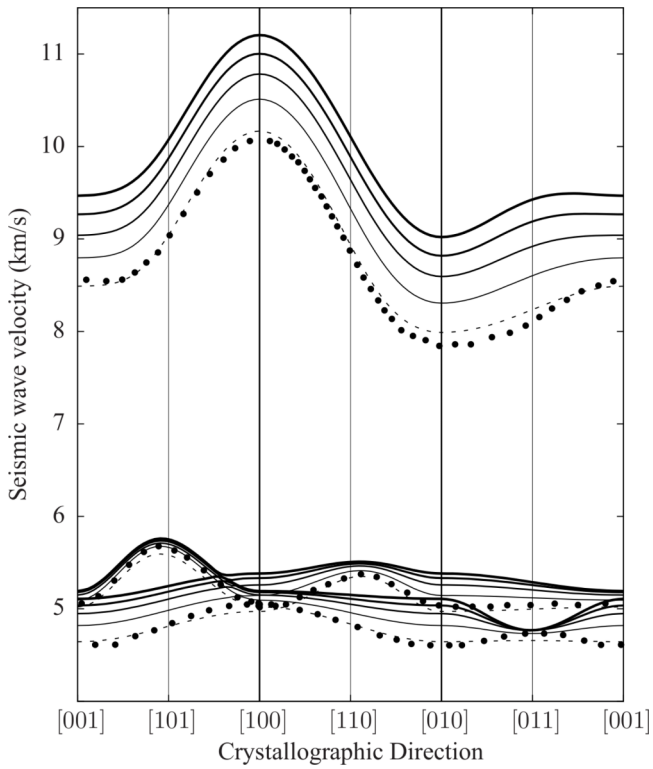


FIG. 3. Directional seismic wave velocities of $Mg_2SiO_4$ forsterite. Zero-pressure computed values are reported as dashed lines and compared with experimental data by Yoneda and Morioka[41] (full circles). Continuous lines of increasing thickness correspond to computed velocities at 5, 10, 15, and 20 GPa. The PBE functional is used for the calculations.

sampled starting from the [001] direction (*i.e.*, the *c* axis), then moving to the [100] one (*a* axis), then to the [010] one (*b* axis), and finally coming back to [001]. Computed values *at zero pressure* are reported as dashed lines and can be compared with experimental directional determinations by Yoneda and Morioka,[41] reported as full circles. We can clearly see how (i) both longitudinal and transverse waves do exhibit a large anisotropy (*i.e.*, large differences as a function of the propagation direction), to be quantified below; (ii) computed values are remarkably superimposed to their experimental counterparts for both $v_p$ and $v_s$; (iii) as regards longitudinal waves, the crystallographic directions of maximum and minimum propagation velocity are the [100] and [010] ones, respectively; (iv) transverse waves show two maxima along directions close to the [101] and [110] ones and minima along [010] and [001]; (v) for all wave polarizations, the (100) plane (*i.e.*, the *bc* plane) is seen to be almost elastically isotropic with small differences in velocity within it, more so for transverse than for longitudinal waves.

As pressure increases (continuous lines of increasing thickness in Figure 3), both longitudinal and transverse seismic wave velocities increase, but in quite different ways. Longitudinal velocities regularly increase (by 13% passing from 0 to 20 GPa) by slightly reducing their azimuthal anisotropy and keeping their profile almost unchanged. Transverse velocities, on the contrary, evolve with pressure by significantly modifying their azimuthal profile: (i) the maximum along the [101] direction remains almost unchanged; (ii) a systematic broadening of the maximum along the [110] direction occurs as pressure passes from 0 to 20 GPa; (iii) a minimum along the [011] direction appears at pressures above about 5 GPa.

In order to quantify the seismic anisotropy of forsterite and its evolution with pressure, let us introduce the following index for the so-called azimuthal anisotropy of quasi-longitudinal and quasi-transverse seismic wave velocities:[13]

$$A_X = \frac{v_{X_{max}} - v_{X_{min}}}{\overline{v}_X}, \tag{9}$$

where $X = p, s$ labels longitudinal and transverse waves and $\overline{v}_X$ is the polycrystalline isotropic average velocity, which can be obtained from the Voigt-Reuss-Hill averaging scheme as[71]

$$\overline{v}_s = \sqrt{\frac{\overline{G}}{\rho}}$$

and

$$\overline{v}_p = \sqrt{\frac{\overline{K} + \frac{4}{3}\overline{G}}{\rho}}, \tag{10}$$

where $\rho$ is the crystal density. For transverse waves, a polarization anisotropy index can be defined, which, given a propagation direction $[hkl]$, measures the difference in speed of fast-transverse and slow-transverse waves,[13]

$$A^{\text{pol}}_{s,[hkl]} = \frac{v^{[hkl]}_{s1} - v^{[hkl]}_{s2}}{\overline{v}_s}. \tag{11}$$

The longitudinal, $A_p$, and transverse, $A_s$, azimuthal anisotropies of forsterite are reported as a function of pressure in the upper and middle panels of Figure 4, respectively.

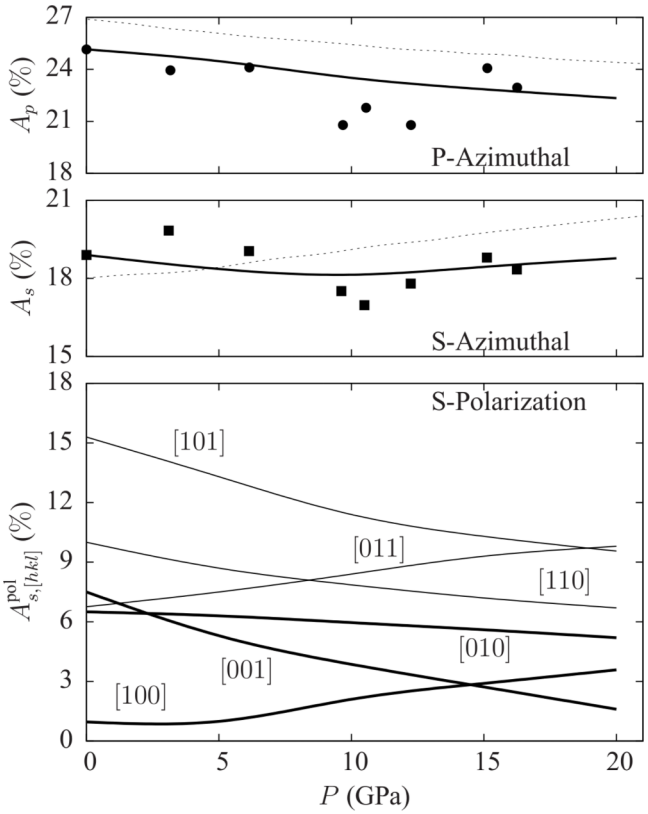


FIG. 4. Azimuthal anisotropy of longitudinal (upper panel) and transverse (middle panel) seismic waves as a function of pressure. Present PBE computed data are given as continuous lines; dashed lines refer to previous LDA theoretical determinations by da Silva *et al.*,[43] while symbols are experimental data by Yoneda and Morioka[41] (zero pressure) and Zha *et al.*[42] (higher pressures). (Lower panel) Directional polarization anisotropy (see Eq. (11)) as a function of pressure.

Experimental data by Yoneda and Morioka[41] and Zha *et al.*[42] are also reported for comparison: (i) experimental values are quite disperse and do not allow for a straightforward identification of a regular trend; (ii) our computed data (continuous lines) show a linear reduction of the longitudinal anisotropy from 25.2% at zero pressure to 22.3% at 20 GPa; (iii) the azimuthal anisotropy of transverse waves is almost constant with pressure (showing a small minimum at about 10 GPa). Despite the overall azimuthal anisotropy of transverse waves remains almost constant (about 18%) with pressure, the polarization anisotropy evolves quite differently along different crystallographic directions. The $A^{\text{pol}}_{s,[hkl]}$ index, introduced with Eq. (11), is given in the lower panel of Figure 4 as a function of pressure for six different crystallographic directions. The polarization anisotropy is seen to significantly increase along [100] (after 5 GPa) and [011], to decrease along [101], [110], and [001], and to remain almost constant, showing just a slight reduction, along [010].

### B. Structural anisotropy and elasticity at upper mantle conditions

In this section, structural and average elastic properties of forsterite are discussed as a simultaneous function of temperature, up to its melting point, and pressure, up to 18 GPa. The effect of the adopted DFT functional on

computed thermal properties (thermal expansion coefficient, equilibrium lattice parameters, and isothermal bulk modulus) is investigated by considering five functionals belonging to three distinct levels of approximation (*i.e.*, three rungs of the so-called "Jacob's ladder"). As expected, different functionals do provide very different absolute values of both equilibrium volume and bulk modulus of forsterite (to be discussed below). However, their descriptions of the thermal expansion and temperature dependence of the bulk modulus are rather close to each other up to the melting point and to the experimental behavior up to about 1500 K, the only exception being the B3LYP hybrid functional that starts deviating above about 800 K. In the upper panel of Figure 5, we report the volumetric thermal expansion coefficient, $\alpha_V(T)$, of forsterite up to 2200 K, its melting temperature being $T_M$ = 2163 K. Six experimental determinations are reported (see caption of Figure 5 for details), which show discrepancies as large as 25% among them. Three experimental datasets that agree particularly well to each other are marked with full (instead of empty) symbols and are here taken as a reference: those from Anderson *et al.*[49] (full circles), Gillet *et al.*[80] (full rhombi), and Fei and Saxena[81] (full triangles). Some considerations on the relative performance of DFT functionals can be made: (i) the description of the thermal expansion of forsterite below 800 K is approximately correct for all functionals; (ii) as already noticed in previous studies on different classes of materials,[28,34,35] the simple LDA functional systematically provides the lowest thermal expansion; (iii) the generalized gradient PBE and PBEsol functionals and the global hybrid PBE0 functional do provide a reliable description of the thermal expansion up to about 1500 K while above that temperature, explicit anharmonic effect is expected to play a non-negligible role in the low-pressure thermal expansion of forsterite; and (iv) the hybrid B3LYP functional provides the largest expansion and significantly deviates from the expected linearity above about 800 K. In the lower panel of Figure 5, we report the isothermal bulk modulus, $K_T$, of forsterite, as computed according to Eq. (7) with the same five functionals and as measured by Anderson *et al.*[49] (full circles) and Suzuki *et al.*[77] (empty circles). Four functionals (LDA, PBE, PBEsol and PBE0) provide a very similar description of the temperature dependence of $K_T$, which almost perfectly matches the experimental slope up to about 1800 K while the B3LYP hybrid functional strongly deviates above about 800 K. As regards the absolute value of the isothermal bulk modulus, the PBEsol and PBE0 functionals are found to provide a satisfactory agreement with the experimental data while PBE and LDA underestimate and overestimate them, respectively.

Let us now discuss the anisotropic thermal expansion of forsterite. Being an orthorhombic crystal, forsterite exhibits three distinct directional thermal expansion coefficients, $\alpha_l$, where $l = a, b, c$ labels the three fundamental lattice vectors. In the three upper panels of Figure 6, $a$, $b$, and $c$ are reported as

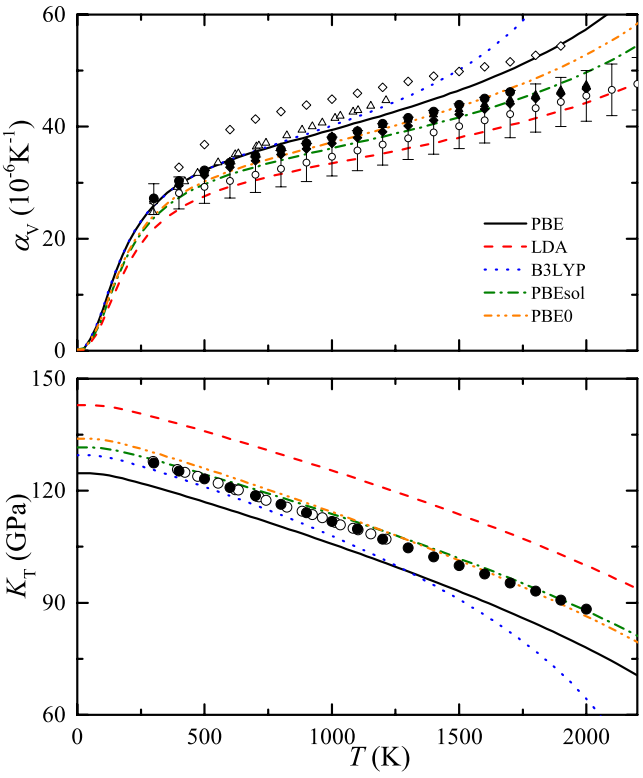


FIG. 5. Upper panel: volumetric thermal expansion coefficient, $\alpha_V(T)$, of forsterite as computed with five DFT functionals and as measured from various experiments; Anderson *et al.*[49] (full circles), Gillet *et al.*[80] (full rhombi), Fei and Saxena[81] (full triangles), Katsura *et al.*[50] (empty rhombi), Suzuki *et al.*[77] (empty triangles), and Bouhifd *et al.*[46] (empty circles). Lower panel: isothermal bulk modulus, $K_T(T)$, of forsterite; experimental data are from Anderson *et al.*[49] (full circles) and Suzuki *et al.*[77] (empty circles).

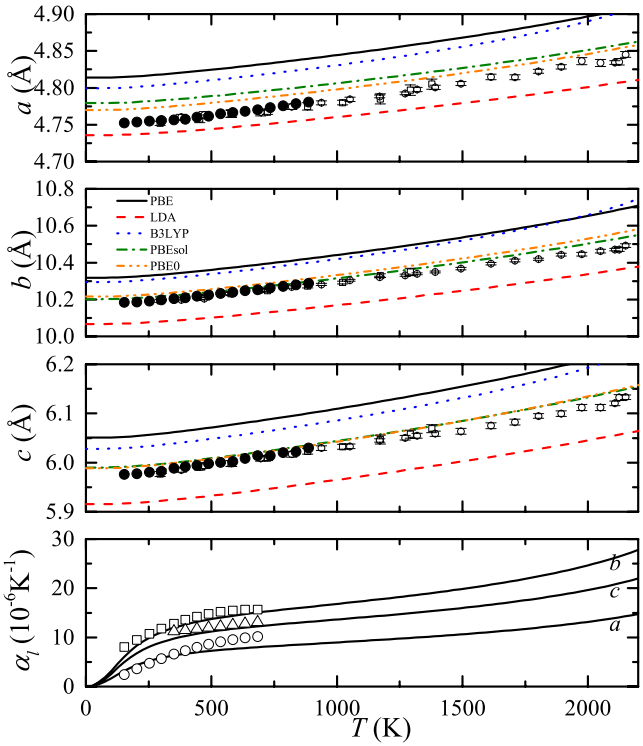


FIG. 6. In the three upper panels, the temperature dependence of the three lattice parameters ($a$, $b$, and $c$) of forsterite is reported. Experimental data from Ye *et al.*[47] (full circles), Bouhifd *et al.*[46] (empty circles), and Hazen[48] (empty squares) are given. Computed data are obtained with the five DFT functionals described in the text. In the lowest panel, the three directional thermal expansion coefficients ($\alpha_a$, $\alpha_b$, and $\alpha_c$) are reported as a function of temperature as computed with the PBE functional (continuous lines) and as derived from experimental data by Ye *et al.*[47] (empty symbols; circles for $\alpha_a$, squares for $\alpha_b$, and triangles for $\alpha_c$).

a function of temperature. Experimental data from Ye *et al.*[47] (full circles), Bouhifd *et al.*[46] (empty circles), and Hazen[48] (empty squares) are reported along with our computed values (with the five DFT functionals). Again, it is clearly seen that the thermal evolution of the cell is reasonably described by all functionals but B3LYP that tends to overestimate the thermal expansion at high temperatures, more so along the *b* crystallographic axis. The LDA functional systematically underestimates all three lattice parameters, B3LYP and PBE do overestimate them while PBEsol and PBE0 do provide the best agreement among them, just slightly overestimating *a*. All adopted functionals do correctly describe the relative thermal expansivity of the three lattice parameters (i.e., $\alpha_b > \alpha_c > \alpha_a$). In the lowest panel of Figure 6, we report these three thermal expansion coefficients, $\alpha_l$, as obtained with the PBE functional (results with other functionals are rather similar and are not shown for sake of clarity) and as derived from experimental data from Ye *et al.*[47] with a third-order polynomial fitting. The agreement is absolutely remarkable thus proving the ability of *ab initio* techniques in describing fine thermal structural features of minerals.

As recalled in the introduction, if high-pressure or high-temperature structural and elastic characterizations of minerals are nowadays routinely accessible from experimental measurements, this is no more the case for simultaneous high-*P*, high-*T* conditions. In this respect, as we shall show below, the combination of first-principle techniques and the QHA does represent an effective strategy to reliably obtain such a description. Equation (6), indeed, allows for computing the pressure-volume-temperature relation of the system. An accurate experimental determination of the *P*-*V*-*T* equation-of-state of forsterite has been reported, as measured in 2009 by Katsura *et al.*[50] with *in situ* X-ray diffraction, to compare with; pressures up to 14 GPa and temperatures up to 1900 K were considered in that study. The *P*-*V*-*T* equation-of-state of forsterite is here reported in Figure 7, where experimental data by Katsura *et al.*[50] are given as full symbols and our computed values, at the PBE level of theory, are given as continuous lines. The $V(P,T)/V_0$ ratio is reported as a continuous function of pressure at 11 different temperatures, $V_0$ being the equilibrium volume at zero pressure and 300 K for both theory and experiment. Apart from a slight underestimation of the volume at simultaneous low-temperatures (up to 500 K) and high-pressures (above 7 GPa), the agreement between the computed and measured volume evolutions is extremely satisfactory in the whole range of explored temperatures and pressures, which is a remarkable finding as it proves the relatively simple QHA to be a reliable approach for the investigation of structural features of olivine minerals at earth's upper mantle conditions. The dashed line in the figure corresponds to the "cold," purely electronic, *P*-*V* equation-of-state of forsterite, as computed at 0 K by neglecting zero-point energy (ZPE) effects. A comparison with the black continuous line, which corresponds to 0 K with inclusion of the ZPE term, shows that ZPE significantly affects the equilibrium structure (by 1%), to an extent which is comparable to a temperature change of about 500 K. Figure 7 is meant to show the excellent agreement that is obtained at temperatures and pressures of the earth's upper mantle between experimental

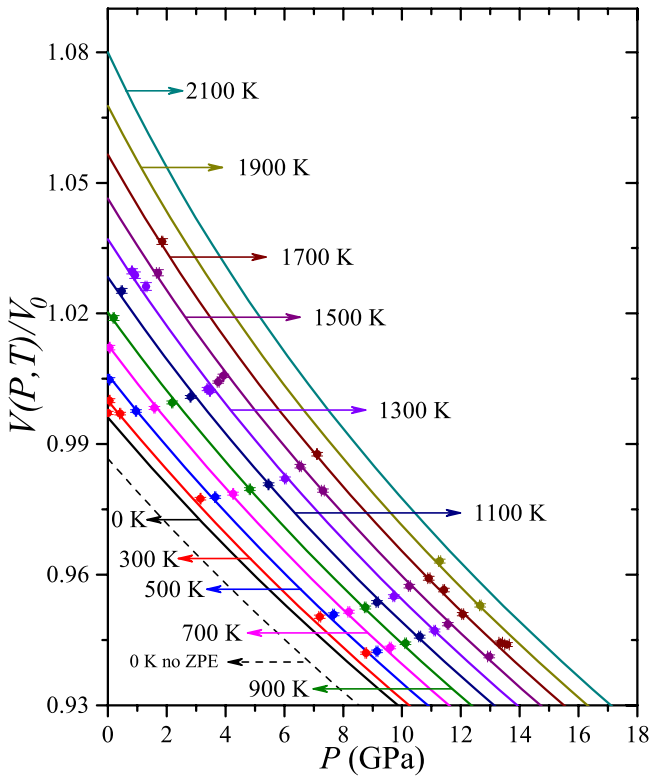


FIG. 7. Pressure-volume-temperature relation of $Mg_2SiO_4$ forsterite, as computed at PBE level in the present study (continuous lines) and as experimentally determined by Katsura *et al.*[50] with *in situ* X-ray diffraction measurements (symbols). The $V(P,T)/V_0$ ratio is reported as a continuous function of pressure at 11 different temperatures, where $V_0$ is the equilibrium volume at zero pressure and 300 K. The dashed line represents the *P*-*V* relation as computed at 0 K without including ZPE effects.

and computed data. Let us now have a closer look at the pressure dependence of the thermal expansion in $Mg_2SiO_4$ forsterite, in particular by explicitly analyzing its anisotropic behavior. In the upper panel of Figure 8, we report the three directional thermal expansion coefficients, $\alpha_l$, corresponding to the three direct lattice vectors, at six different pressures (from 0 to 10 GPa, in steps of 2 GPa). We can clearly see that (i) at all temperatures and pressures, their relative order is unchanged, with $\alpha_b > \alpha_c > \alpha_a$; (ii) as pressure increases, the high-temperature part of the curves becomes more linear as anharmonic contributions to the thermal expansion are rapidly suppressed; and (iii) pressure is affecting mostly the *b* axis, followed by the *c* one, while the thermal expansion along the *a* axis is the least affected.

The simultaneous dependence on temperature and pressure of the isothermal bulk modulus, $K_T$, of forsterite is given in the lower panel of Figure 8 (continuous lines). The isothermal bulk modulus is computed as a Helmholtz free energy second derivative (see Eq. (7)) and can be compared with measurements from X-ray diffraction experiments, for instance. In the figure, full symbols are experimental data of $K_T$ as measured by Anderson *et al.*[49] (circles) and Suzuki *et al.*[77] (triangles). All computed values, as obtained at PBE level, are upshifted by 6.2 GPa in the figure, in order to match their experimental counterparts as we want to highlight the correctness of their temperature (and pressure) dependence

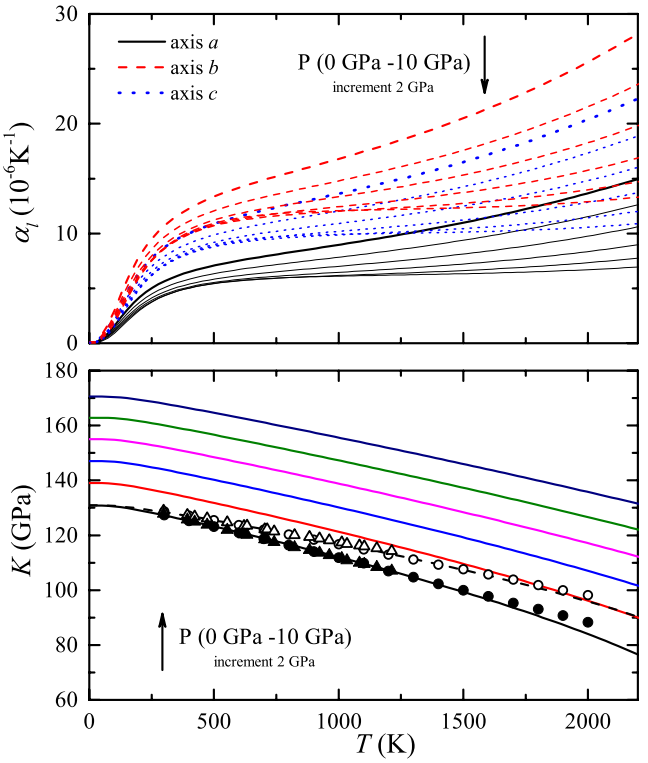


FIG. 8. Upper panel: directional thermal expansion coefficients, $\alpha_l$, where $l = a, b, c$, as a continuous function of temperature, at six pressures (0, 2, 4, 6, 8, and 10 GPa). Lower panel: isothermal bulk modulus, $K_T$ (continuous lines). At zero pressure, the adiabatic bulk modulus, $K_S$, is also reported (dashed line). Computed bulk modulus values are upshifted by 6.2 GPa. Isothermal (full symbols) and adiabatic (empty symbols) experimental data at zero pressure are from Anderson *et al.*[49] (circles) and Suzuki *et al.*[77] (triangles). The PBE level of theory is used for all computed data.

rather than of their absolute values, which are rather DFT functional-dependent, as previously shown in Figure 5. By comparing with the experiments at zero pressure, we see how the quasi-harmonic description of forsterite allows for reliably describing the thermal dependence of its bulk modulus up to about 1800 K, which is a remarkable achievement. The computed $K_T$ is then reported at five other pressures, up to 10 GPa (see below for a more quantitative analysis). Some experimental techniques for measuring the bulk modulus of a crystal, other than X-ray diffraction experiments which naturally allow for the system to thermally equilibrate, involve elastic waves and are characterized by very short time scales that prevent the system from reaching a thermal equilibrium; in these cases, an adiabatic bulk modulus, $K_S$, is measured instead of $K_T$. Adiabatic and isothermal bulk moduli do obviously coincide with each other at zero temperature, $K_S$ always being larger than $K_T$ at any finite temperature. According to the QHA, the adiabatic bulk modulus can be derived from its isothermal counterpart as

$$K_S(T) = K_T(T) + \frac{\alpha_V(T)^2 V(T) T K_T(T)^2}{C_V(T)}, \qquad (12)$$

where $C_V$ is the constant-volume specific heat of the system as computed with standard statistical thermodynamics from the phonon frequencies.[35] Computed values of the adiabatic bulk modulus at zero pressure are reported in the figure as dashed lines and compared with available experimental determinations (empty symbols). Again the description of both the absolute value of the $K_S - K_T$ difference at all temperatures and, accordingly, of the $K_S$ dependence on temperature is found to be described very accurately within the QHA.

TABLE II. Isothermal bulk modulus of $Mg_2SiO_4$ forsterite at zero pressure, $K_T^0$, and its first-, $dK_T/dP$, and second-derivatives, $d^2K_T/dP^2$, with respect to pressure at various temperatures. All values computed at the PBE level of theory; $K_T^0$ values are upshifted by 6.2 GPa and correspond to those reported in Figure 8.

| $T$ (K) | $K_T^0$ (GPa) | $dK_T/dP$ | $d^2K_T/dP^2$ (GPa$^{-1}$) |
|---|---|---|---|
| 0 | 131 | 4.13 | −0.026 |
| 300 | 127 | 4.22 | −0.031 |
| 500 | 123 | 4.32 | −0.036 |
| 700 | 119 | 4.43 | −0.043 |
| 900 | 114 | 4.55 | −0.051 |
| 1100 | 110 | 4.70 | −0.062 |
| 1300 | 105 | 4.89 | −0.076 |
| 1500 | 99 | 5.12 | −0.095 |
| 1700 | 94 | 5.42 | −0.121 |
| 1900 | 88 | 5.80 | −0.157 |
| 2100 | 81 | 6.31 | −0.208 |

First and second pressure derivatives of the isothermal bulk modulus, at several temperatures, are key quantities for the geophysical characterization of the earth's deep interior and are extremely difficult to be determined experimentally. In order to be as quantitative as possible in this respect, we introduce Table II where we report at 11 distinct temperatures (in the range 0–2100 K), the absolute value of the zero-pressure isothermal bulk modulus, $K_T^0$, its first pressure derivative, $K_T' \equiv dK_T/dP$, and its second pressure derivative, $K_T'' \equiv d^2K_T/dP^2$, as computed at the PBE level of theory. Regular trends of both $K_T'$ and $K_T''$ are found as a function of temperature. The first-order pressure derivative of the bulk modulus significantly increases as temperature is increased: it passes from 4.13 at 0 K to 6.31 at 2100 K. The second-order pressure derivative is always negative and its absolute value dramatically increases by about one order of magnitude as temperature passes from 0 to 2100 K.

## IV. CONCLUSIONS

The elastic anisotropy of forsterite has been characterized under pressures up to 20 GPa with *ab initio* theoretical simulations. The evolution with pressure of directional seismic wave velocities and seismic anisotropy (azimuthal and polarization) has been determined. From quasi-harmonic calculations, the *P-V-T* equation-of-state, the anisotropic thermal expansion coefficients, and the bulk modulus dependence on temperature and pressure have been accurately predicted at earth's upper mantle conditions of simultaneous high pressure and temperature. By comparison with available experimental data, the quasi-harmonic approximation is found to provide a reliable description of all properties in the whole stability domain of forsterite, 0–14 GPa of pressure and 0–1500 K of temperature, which is a remarkable success of such a relatively simple

scheme. These results prove the reliability and effectiveness of DFT quasi-harmonic simulations in predicting high-pressure high-temperature properties of minerals of geophysical interest.

The temperature dependence of the elastic anisotropy of forsterite has not yet been addressed in the present study as it requires a full thermoelastic characterization of the system (i.e., evaluation of the elastic tensor at several temperatures) for which new algorithms are currently being implemented into the CRYSTAL program by some of the present authors.

## ACKNOWLEDGMENTS

J.M. acknowledges the Brazilian scholarship program "Ciência sem Fronteiras" (Process No. 248425/2013-7/SWE).

[1]R. Dovesi, B. Civalleri, C. Roetti, V. R. Saunders, and R. Orlando, Rev. Comput. Chem. **21**, 1 (2005).
[2]S. Baroni, S. de Gironcoli, A. D. Corso, and P. Giannozzi, Rev. Mod. Phys. **73**, 515 (2001).
[3]S. Grimme, J. Antony, S. Ehrlich, and H. Krieg, J. Chem. Phys. **132**, 154104 (2010).
[4]C. Pisani, *Quantum-Mechanical Ab Initio Calculation of the Properties of Crystalline Materials*, Lecture Notes in Chemistry Series Vol. 67 (Springer Verlag, Berlin, 1996).
[5]R. Dronskowski, *Computational Chemistry of Solid State Materials* (Wiley, Weinheim, 2005).
[6]R. Dovesi, R. Orlando, A. Erba, C. M. Zicovich-Wilson, B. Civalleri, S. Casassa, L. Maschio, M. Ferrabone, M. De La Pierre, Ph. D'Arco *et al.*, Int. J. Quantum Chem. **114**, 1287 (2014).
[7]E. Zurek and W. Grochala, Phys. Chem. Chem. Phys. **17**, 2917 (2015).
[8]A. B. Alchagirov, J. P. Perdew, J. C. Boettger, R. C. Albers, and C. Fiolhais, Phys. Rev. B **63**, 224115 (2001).
[9]R. E. Cohen, O. Gülseren, and R. J. Hemley, Am. Mineral. **85**, 338 (2000).
[10]I. Souza and J. Martins, Phys. Rev. B **55**, 8733 (1997).
[11]K. Doll, Mol. Phys. **108**, 223 (2010).
[12]B. B. Karki, G. J. Ackland, and J. Crain, J. Phys.: Condens. Matter **9**, 8579 (1997).
[13]B. B. Karki, L. Stixrude, and R. M. Wentzcovitch, Rev. Geophys. **39**, 507, doi:10.1029/2000RG000088 (2001).
[14]J. Wang, J. Li, S. Yip, S. Phillpot, and D. Wolf, Phys. Rev. B **52**, 12627 (1995).
[15]A. Erba, A. Mahmoud, D. Belmonte, and R. Dovesi, J. Chem. Phys. **140**, 124703 (2014).
[16]N. W. Ashcroft and N. D. Mermin, *Solid State Physics* (Saunders College, Philadelphia, USA, 1976).
[17]S. Baroni, P. Giannozzi, and E. Isaev, Rev. Mineral. Geochem. **71**, 39 (2010).
[18]R. E. Allen and F. W. De Wette, Phys. Rev. **179**, 873 (1969).
[19]L. L. Boyer, Phys. Rev. Lett. **42**, 584 (1979).
[20]D. Mainprice, G. Barruol, and W. Ben Ismail, *The Seismic Anisotropy of the Earth's Mantle: From Single Crystal to Polycrystal* (American Geophysical Union, 2013), pp. 237–264.
[21]A. E. Ringwood, *Composition and Petrology of the Earth's Mantle* (McGraw-Hill, New York, 1975).
[22]J. D. Bass and D. L. Anderson, Geophys. Res. Lett. **11**, 229, doi:10.1029/GL011i003p00229 (1984).
[23]D. L. Anderson and J. D. Bass, Nature **320**, 321 (1986).
[24]T. S. Duffy and D. L. Anderson, J. Geophys. Res. **94**, 1895, doi:10.1029/JB094iB02p01895 (1989).
[25]E. Knittle, in *A Handbook of Physical Constants: Mineral Physics and Crystallography*, edited by T. J. Ahrens (AGU, Washington D. C., 1995), Vol. 2, pp. 98–142.
[26]F. Jiang, S. Speziale, and T. S. Duffy, J. Geophys. Res. **109**, B10210, doi:10.1029/2004JB003081 (2004).
[27]B. B. Karki, R. M. Wentzcovitch, S. de Gironcoli, and S. Baroni, Science **286**, 1705 (1999).
[28]A. Erba, J. Maul, R. Demichelis, and R. Dovesi, Phys. Chem. Chem. Phys. **17**, 11670-11677 (2015).
[29]D. Mainprice and A. Nicolas, J. Struct. Geol. **11**, 175 (1989).
[30]D. L. Anderson, *Theory of the Earth* (Blackwell Scientific Publications, Boston, 1989).
[31]S. I. Karato, Pure Appl. Geophys. **151**, 565 (1998).
[32]A. M. Dziewonski and D. L. Anderson, Phys. Earth Planet. Inter. **25**, 297 (1981).
[33]J. P. Perdew and K. Schmidt, AIP Conf. Proc. **577**, 1 (2001).
[34]A. Erba, J. Chem. Phys. **141**, 124115 (2014).
[35]A. Erba, M. Shahrokhi, R. Moradian, and R. Dovesi, J. Chem. Phys. **142**, 044114 (2015).
[36]A. Erba and R. Dovesi, Phys. Rev. B **88**, 045121 (2013).
[37]A. Erba, K. E. El-Kelany, M. Ferrero, I. Baraille, and M. Rérat, Phys. Rev. B **88**, 035102 (2013).
[38]A. Mahmoud, A. Erba, K. E. El-Kelany, M. Rérat, and R. Orlando, Phys. Rev. B **89**, 045103 (2014).
[39]A. Erba, A. Mahmoud, R. Orlando, and R. Dovesi, Phys. Chem. Miner. **41**, 151 (2014).
[40]H. Shimizu, W. A. Bassett, and E. M. Brody, J. Appl. Phys. **53**, 620 (1982).
[41]A. Yoneda and M. Morioka, Geophys. Monogr. Ser. **67**, 207, doi:10.1029/gm067p0207 (1992).
[42]C.-S. Zha, T. S. Duffy, R. T. Downs, H.-K. Mao, and R. J. Hemley, J. Geophys. Res. **101**, 17535, doi:10.1029/96JB01266 (1996).
[43]C. da Silva, L. Stixrude, and R. M. Wentzcovitch, Geophys. Res. Lett. **24**, 1963, doi:10.1029/97GL01756 (1997).
[44]P. T. Jochym, K. Parlinski, and P. Krzywiec, Comput. Mater. Sci. **29**, 414 (2004).
[45]M. Nunez-Valdez, K. Umemoto, and R. M. Wentzcovitch, Geophys. Res. Lett. **37**, L14308, doi:10.1029/2010gl044205 (2010).
[46]M. A. Bouhifd, D. Andrault, G. Fiquet, and P. Richet, Geophys. Res. Lett. **23**, 1143, doi:10.1029/96GL01118 (1996).
[47]Y. Ye, R. A. Schwering, and J. R. Smyth, Am. Mineral. **94**, 899 (2009).
[48]R. M. Hazen, Am. Mineral. **61**, 1280 (1976).
[49]O. L. Anderson, D. Isaak, and H. Oda, Rev. Geophys. **30**, 57, doi:10.1029/91RG02810 (1992).
[50]T. Katsura, A. Shatskiy, M. G. M. Manthilake, S. Zhai, H. Fukui, D. Yamazaki, T. Matsuzaki, A. Yoneda, E. Ito, A. Kuwata *et al.*, Phys. Earth Planet. Inter. **174**, 86 (2009).
[51]L. Li, R. M. Wentzcovitch, D. J. Weidner, and C. R. S. Da Silva, J. Geophys. Res. **112**, B05206, doi:10.1029/2006jb004546 (2007).
[52]G. Ottonello, B. Civalleri, J. Ganguly, M. Vetuschi Zuccolini, and Y. Nöel, Phys. Chem. Miner. **36**, 87 (2009).
[53]M. De La Pierre, R. Orlando, L. Maschio, K. Doll, P. Ugliengo, and R. Dovesi, J. Comput. Chem. **32**, 1775 (2011).
[54]R. Demichelis, B. Civalleri, M. Ferrabone, and R. Dovesi, Int. J. Quantum Chem. **110**, 406 (2010).
[55]J. C. Slater, Phys. Rev. **81**, 385 (1951).
[56]S. H. Vosko, L. Wilk, and M. Nusair, Can. J. Phys. **58**, 1200 (1980).
[57]J. P. Perdew, K. Burke, and M. Ernzerhof, Phys. Rev. Lett. **77**, 3865 (1996).
[58]J. Perdew, A. Ruzsinsky, G. I. Csonka, O. A. Vydrov, G. E. Scuseria, L. A. Constantin, X. Zhou, and K. Burke, Phys. Rev. Lett. **100**, 136406 (2008).
[59]A. D. Becke, J. Chem. Phys. **98**, 5648 (1993).
[60]C. Adamo and V. Barone, J. Chem. Phys. **110**, 6158 (1999).
[61]R. Dovesi, V. R. Saunders, C. Roetti, R. Orlando, C. M. Zicovich-Wilson, F. Pascale, K. Doll, N. M. Harrison, B. Civalleri, I. J. Bush *et al.*, CRYSTAL14 User's Manual, Università di Torino, Torino, 2014, http://www.crystal.unito.it.
[62]K. Doll, R. Dovesi, and R. Orlando, Theor. Chem. Acc. **112**, 394 (2004).
[63]K. Doll, R. Dovesi, and R. Orlando, Theor. Chem. Acc. **115**, 354 (2006).
[64]W. F. Perger, J. Criswell, B. Civalleri, and R. Dovesi, Comput. Phys. Commun. **180**, 1753 (2009).
[65]A. Erba, M. Ferrabone, J. Baima, R. Orlando, M. Rérat, and R. Dovesi, J. Chem. Phys. **138**, 054906 (2013).
[66]D. C. Wallace, *Thermodynamics of Crystals* (Wiley, New York, USA, 1972).
[67]D. C. Wallace, Rev. Mod. Phys. **37**, 57 (1965).
[68]A. Mahmoud, A. Erba, K. Doll, and R. Dovesi, J. Chem. Phys. **140**, 234703 (2014).
[69]A. Erba, A. M. Navarrete-López, V. Lacivita, P. D'Arco, and C. M. Zicovich-Wilson, Phys. Chem. Chem. Phys. **17**, 2660 (2015).
[70]J. F. Nye, *Physical Properties of Crystals* (Oxford University Press, Oxford, 1957).

[71]G. Ottonello, B. Civalleri, J. Ganguly, W. F. Perger, D. Belmonte, and M. Vetuschi Zuccolini, Am. Mineral. **95**, 563 (2010).
[72]J. C. Tan, B. Civalleri, A. Erba, and E. Albanese, CrystEngComm **17**, 375 (2015).
[73]A. Erba, M. Ferrabone, R. Orlando, and R. Dovesi, J. Comput. Chem. **34**, 346 (2013).
[74]K. Parlinski, Z. Q. Li, and Y. Kawazoe, Phys. Rev. Lett. **78**, 4063 (1997).
[75]A. Togo, F. Oba, and I. Tanaka, Phys. Rev. B **78**, 134106 (2008).
[76]R. Hill, J. Mech. Phys. Solids **11**, 357 (1963).
[77]I. Suzuki, O. L. Anderson, and Y. Sumino, Phys. Chem. Miner. **10**, 38 (1983).
[78]M. J. P. Musgrave, *Crystal Acoustics* (Holden-Day, San Francisco, California, 1970).
[79]B. A. Auld, *Acoustic Fields and Waves in Solids* (Krieger Publishing Company, Malabar, Florida, 1973).
[80]P. Gillet, P. Richet, F. Guyot, and G. Fiquet, J. Geophys. Res. **96**, 11805, doi:10.1029/91JB00680 (1991).
[81]Y. Fei and S. Saxena, Phys. Chem. Miner. **13**, 311 (1986).